Electronic Supplementary Material (ESI) for Inorganic Chemistry Frontiers.

Electronic Supplementary Information

A highly connected metal-organic framework with a specific nonpolar nanotrap for inverse ethane/ethylene separation

Jing-Jing Pang, Zhi-Han Ma, Qiang-Qiang Yang, Kuo Zhang, Xin Lian, Hongliang Huang,* Zhao-Quan Yao,* Baiyan Li, Jian Xu* and Xian-He Bu

*To whom corresponding should be addressed. Email: huanghongliang@tiangong.edu.cn; yaozq@email.tjut.edu.cn; jxu@nankai.edu.cn

Table of Contents

Section S1: Methods.

Materials and instrumentation.

All the chemicals and reagents were purchased commercially and used without purification. *N*,*N*'-dimethylformamide (DMF), acetone, Ether, CH_3OH, and CH_2Cl_2 were obtained from Concord Technology (Tianjin). H_4TCPE ligand was purchased from Bide Pharmatech. $Tb(NO_3)_3{\cdot}6H_2O$ and 2-fluorobenzoic acid were obtained from Aladdin. Room temperature ^{1}H NMR and ^{13}C NMR spectra were carried out on a Bruker Avance NEO 400MHz NMR spectrometer at 400 and 100 MHz, respectively. Chemical shifts, δ, were reported in ppm relative to the internal standard TMS for ^{1}H NMR. Fourier transform infrared (FT-IR) spectra (KBr) were obtained using a Bruker TENSOR 37 fourier transform infrared spectrophotometer. Powder X-ray diffraction (PXRD) patterns were collected on the Rigaku Miniflex 600 at 40 kV, 15 mA with a Cu target tube (λ = 1.54178) at room temperature in the range 3° ≤ 2θ ≤ 50°. Elemental analyses (EA) were measured by Vario Elementar Cube elemental analyzer. Thermogravimetric analyses (TGA) were carried out on a Rigaku standard TG-DTA analyzer in the range from room temperature to 800 °C at a heating rate of 10 °C/min, with an empty Al_2O_3 crucible used as the reference. Nitrogen adsorption-desorption isotherm were measured by using a Micrometrics ASAP 2460 volumetric gas adsorption analyzer. The hydrocarbon sorption measurements were performed on an automatic volumetric adsorption apparatus Micromeritics ASAP 2020 surface area analyzer. The experimental temperatures of 273 and 298 K were maintained by ice-water bath and water bath, respectively.

X-ray crystal structure determination.

Single-crystal X-ray diffraction (SCXRD) data was collected with Bruker D8 Venture Single Crystal X-ray Diffraction using mirror-monochromated Ga-Kα radiation (λ = 1.34139 Å) at 193 K. All the structures were solved by SHELXT program of the SHELXTL package and refined with SHELXL.[1] Hydrogen atoms on organic ligands were generated by the riding mode. The program SQUEEZE,[2] a part of the PLATON package of crystallographic software, was used to calculate the solvent-accessible area and remove their contributions to the overall intensity data. Simulation of the PXRD pattern was carried out by the single-crystal data and diffraction-crystal module of the Mercury program available free of charge via http://www.iucr.org.

Dynamic breakthrough experiments.

The dynamic breakthrough curves were measured using the Multi-component Adsorption Breakthrough Curve Analyzer (BSD-MAB). Firstly, the activated sample was extruded by the tablet machine, then ground and sieved by the 40-60 screen mesh, from which it was put into the tube (φ 6 mm × 60 mm). Next, the He gas flow was pumped into the adsorption bed for 5 h at 150°C in order to expel other gases. Finally, at the ambient condition, the C_2H_6/C_2H_4 binary mixed gases (10/90 and 50/50, v/v) with He as the carrier gas (50% and 80%, vol%) were passed through the adsorption bed at a total inlet flow rate of 10 mL/min. The gas concentrations of effluents were monitored by on-line mass spectrometry

continuously until the breakthrough was completed. After the first breakthrough cycle, the adsorbent was regenerated conveniently by heating at 150 °C under He flow for 5 h to complete three continuous breakthrough cycles.

Isosteric enthalpy of adsorption.

Isosteric enthalpy of adsorption (Q_{st}) was derived from the adsorption data using the viral equation[3]:

$$\ln(P) = \ln(N) + \frac{1}{T}\sum_{i=0}^{m} a_i N^i + \sum_{j=0}^{n} b_j N^j$$

where P is pressure, N denotes the amount adsorbed at pressure P, T is temperature, m and n refer to the number of terms required to adequately describe the isotherm, and a_i and b_j are empirical parameters.

Ideal adsorption solution theory (IAST) calculations.

The C_2H_6 and C_2H_4 adsorption isotherms at 298 K were fitted by a dual-site Langmuir-Freundlich model:

$$q = q_A \frac{b_A p^{vA}}{1 + b_A p^{vA}} + q_B \frac{b_B p^{vB}}{1 + b_B p^{vB}}$$

where p(kPa) is the pressure of the gas phase and the adsorbed phase at equilibrium, q is the adsorbed amount per mass of adsorbent (mmol/g), q_A and q_B are the saturation adsorption amount of site A and B (mmol/g), b_A and b_B are the affinity coefficients of site A and B (kPa), and v_A and v_B represent the deviations from an ideal homogeneous surface. The fitting parameters were utilized to predict the IAST adsorption selectivity, which is defined as follows:

$$S = \frac{q_1 p_2}{q_2 p_1}$$

where S represents the adsorption selectivity, q_1 and q_2 are the gas adsorption capacities of component 1 and 2, p_1 and p_2 refer to the partial pressure of component 1 and 2, respectively.

Theoretical calculations.

DFT calculations were carried out using the CP2K code.[4] All calculations employed a mixed Gaussian and planewave basis sets. Core electrons were represented with norm-conserving Goedecker-Teter-Hutter pseudopotentials,[5-7] and the valence electron wavefunction was expanded in a double-zeta basis set with polarization functions[8] along with an auxiliary plane wave basis set with an energy cutoff of 360 Ry. The generalized gradient approximation exchange-correlation functional of Perdew, Burke, and Enzerhof (PBE)[9] was used. Each configuration was optimized with the Broyden-Fletcher-Goldfarb-Shanno (BGFS) algorithm with SCF convergence criteria of 1.0×10^{-8} a.u. To compensate the long-range van der Waals dispersion interaction between the adsorbate and **NKU-200-Tb**, the DFT-D3 scheme[10] with an empirical damped potential term was added into the energies obtained from exchange correlation functional in all calculations. The static binding energies between the adsorbate and the **NKU-200-Tb** were calculated using the following equation:

$$\Delta E = E_{adsorbate@MOF} - E_{MOF} - E_{adsorbate}$$

$E_{adsorbate@MOF}$ and E_{MOF} represent the total energies of **NKU-200-Tb** with and without the adsorbate, respectively. $E_{adsorbate}$ is the total energy of the adsorbate.

Section S2: Synthesis of NKU-200-Tb.

Characterization of H_4TCPE.

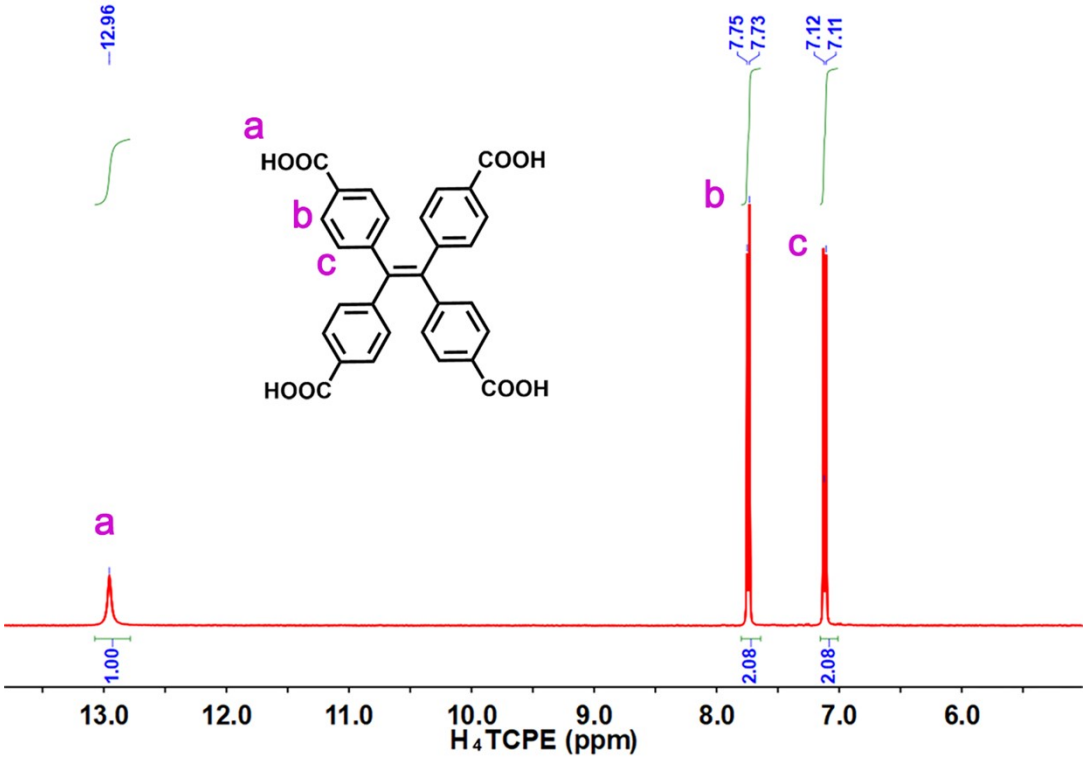

Fig. S1 The ^{1}H NMR spectrum of H_4TCPE.

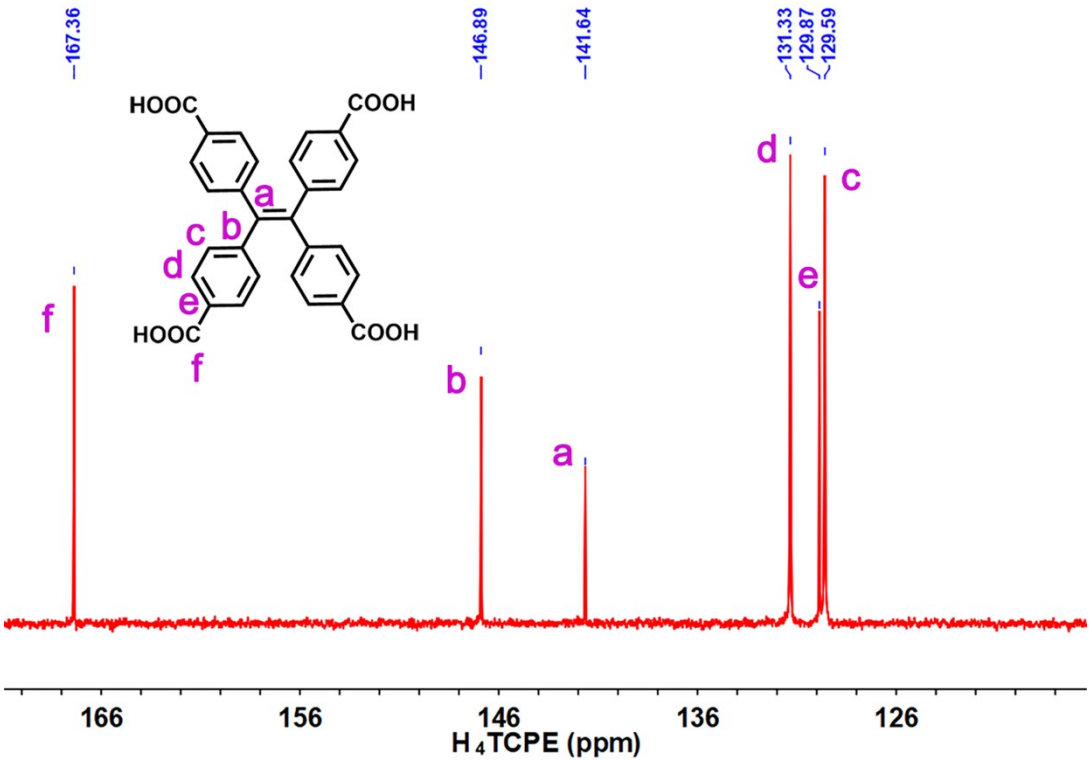

Fig. S2 The ^{13}C NMR spectrum of H_4TCPE.

Synthesis of NKU-200-Tb: $[Tb_9(\mu_3\text{-}O)_2(\mu_3\text{-}OH)_{12}(H_2O)_9(TCPE)_3]^{-}\cdot[H_3O]^{+}\cdot(solvent)_x$ H_4TCPE ligand (5.1 mg, 0.01 mmol), $Tb(NO_3)_3\cdot 6H_2O$ (18.1 mg, 0.04 mmol), and 2-fluorobenzoic acid (400 mg, 2.85 mmol) were dissolved in DMF (2.0 mL) with HNO_3 (0.3 ml, 3.5 M in DMF) and sealed in a 10 ml glass vial. After 10 min ultrasonication, the mixture was heated in a 110 °C oven for 72 h without disturbance. The colorless hexagonal prism crystals were collected after filtration, washed with DMF for several times, and dried in air. Yield: 40.2%. Elemental analysis (%): calcd: C 32.40; H 2.34; Found: C 33.30; H 2.53. FT-IR spectra (cm^{-1}): 3421 (vs), 1659 (vs), 1600 (vs), 1550 (s), 1415 (vs), 1099 (m), 771 (m).

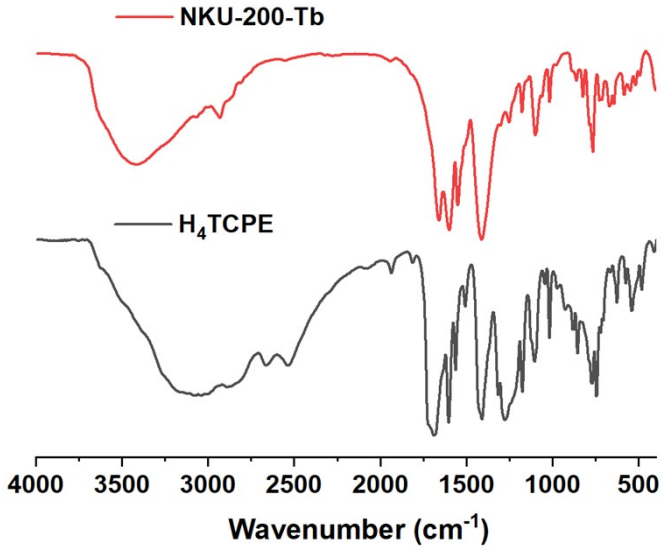

Fig. S3 FT-IR spectra of H_4TCPE ligand and **NKU-200-Tb**.

Section S3: Structure and characterization of NKU-200-Tb.

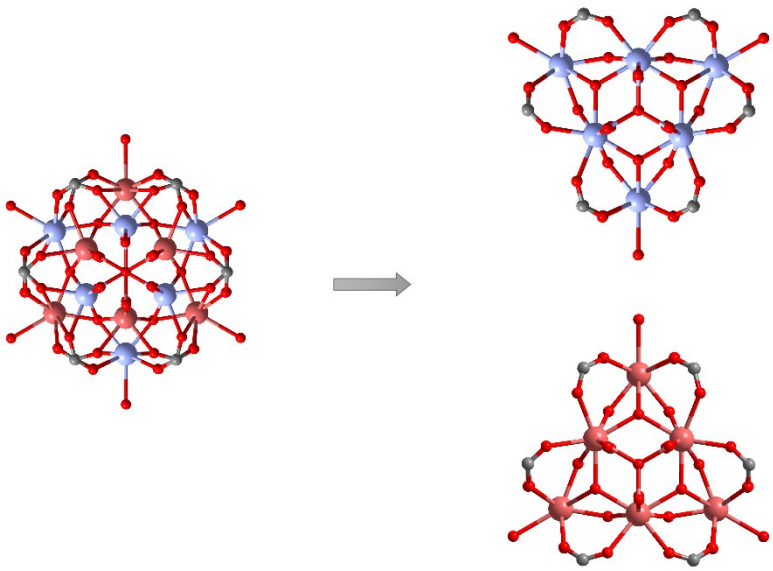

Fig. S4 Representation of the disordered Tb_9 clusters with two sets of positions in **NKU-200-Tb**.

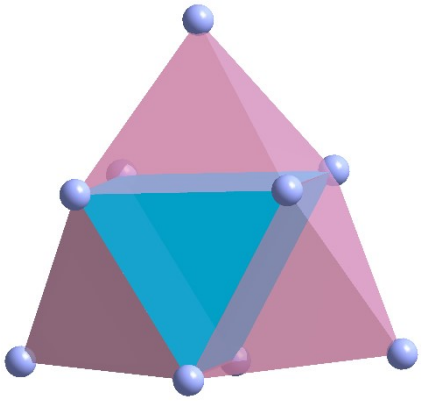

Fig. S5 Representation of nine Tb^{3+} ions of nonanuclear Tb_9 cluster arranged in a tricapped trigonal prism geometry.

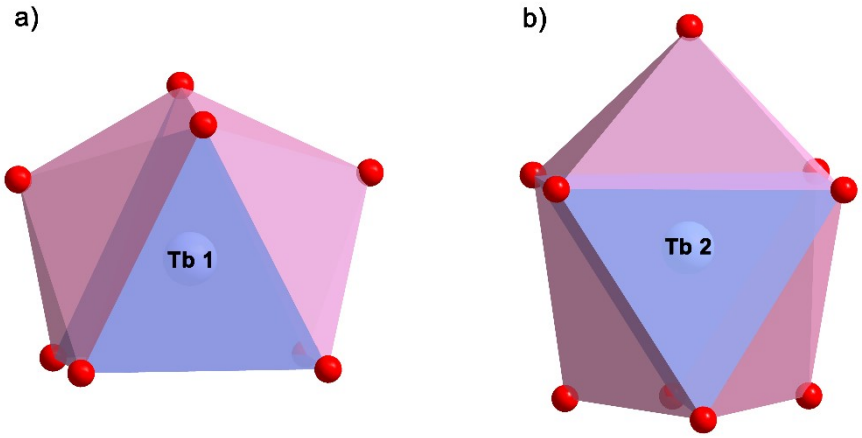

Fig. S6 Coordination environments for the eight-coordinated (a) and nine-coordinated (b) Tb^{3+} ions in **NKU-200-Tb**.

Section S4: Thermal and solvent stability of NKU-200-Tb.

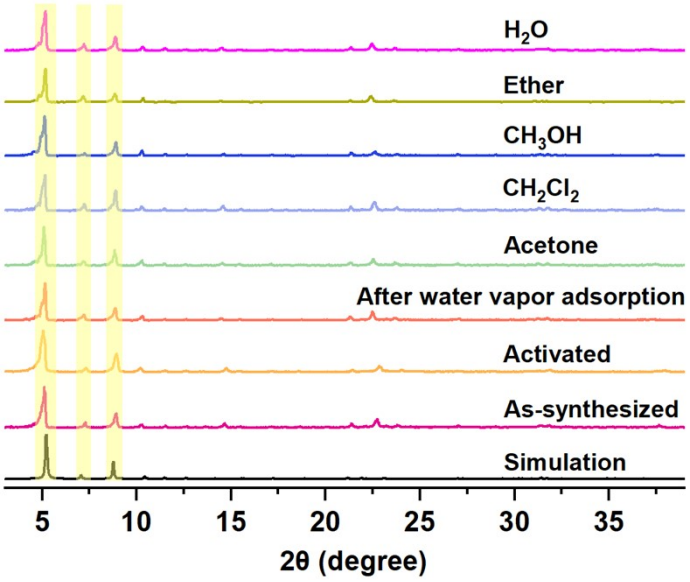

Fig. S7 PXRD patterns of the solvated samples of **NKU-200-Tb** (after soaking in different organic solvents for 24 h) and the activated sample before and after water vapor adsorption.

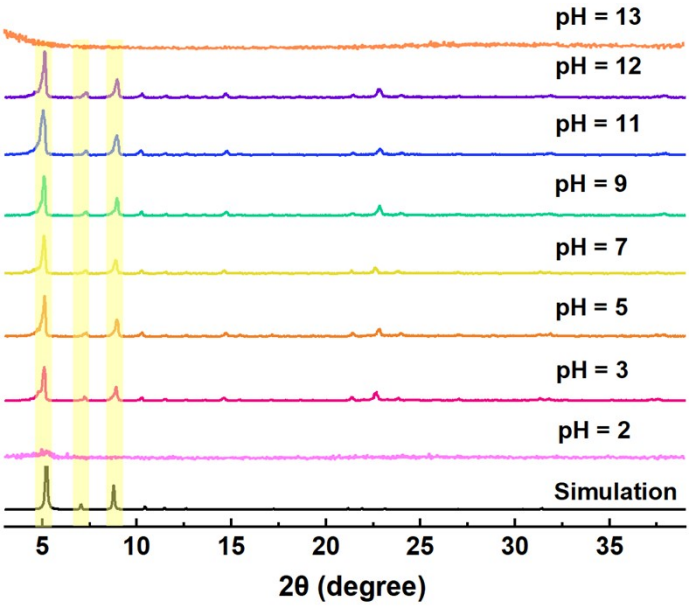

Fig. S8 PXRD patterns of **NKU-200-Tb** after immersion in the aqueous solutions with a broad pH range of 2 – 13 for 24 h.

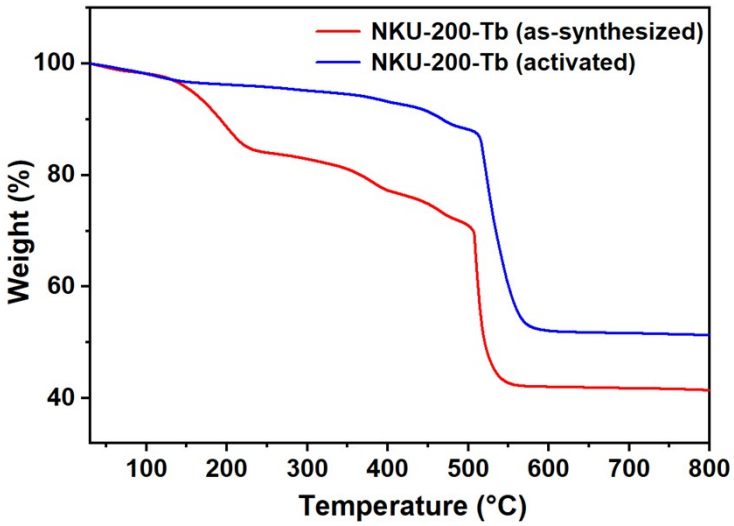

Fig. S9 TGA curves of the as-synthesized and activated samples of **NKU-200-Tb**.

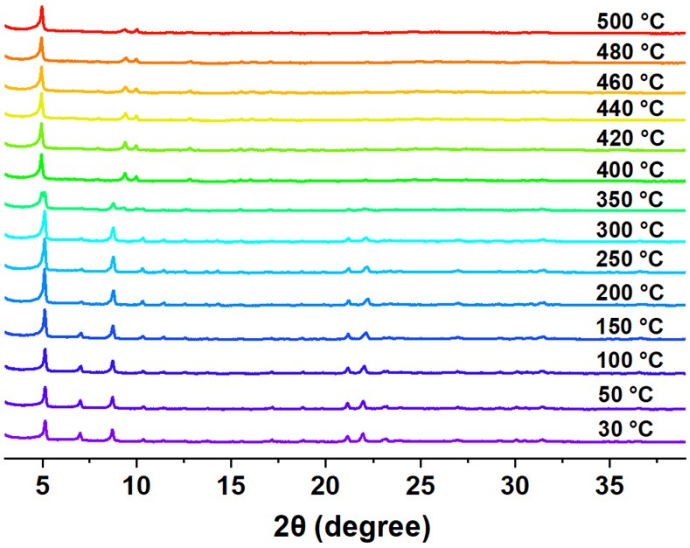

Figure S10. Variable-temperature PXRD patterns of the as-synthesized sample of **NKU-200-Tb**.

Section S5: Gas adsorption measurements and analysis.

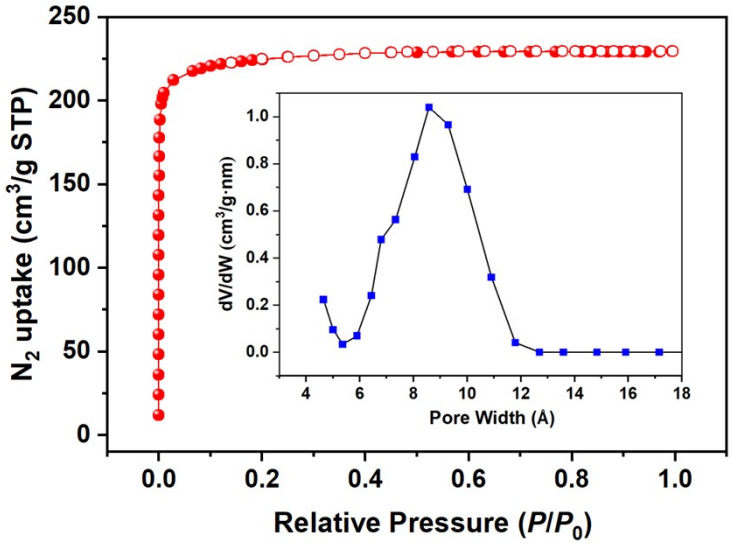

Fig. S11 N_2 adsorption-desorption isotherm on **NKU-200-Tb** at 77 K. Inset: the pore size distribution profile.

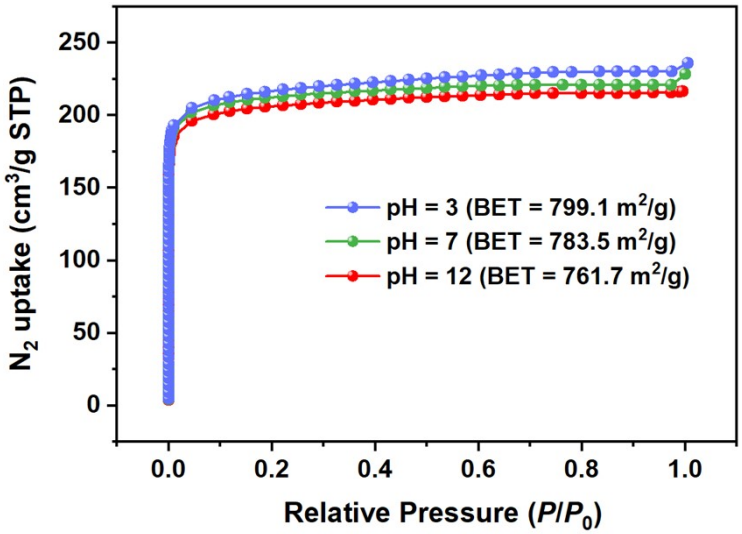

Fig. S12 N_2 adsorption isotherms on **NKU-200-Tb** after soaking the sample into the aqueous solutions with the pH value of 3, 7, and 12 for 12 h. No significant reduction in the N_2 adsorption amount and BET surface area was found, excluding the degradation of its porous structure under these harsh conditions.

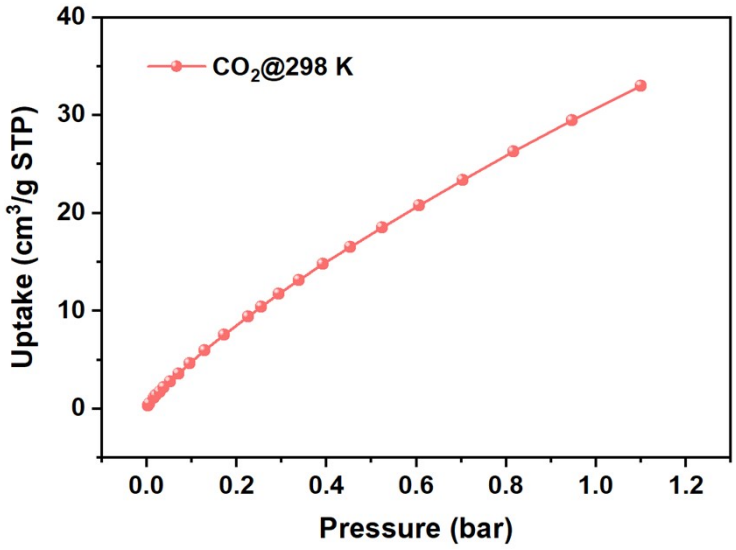

Fig. S13 The adsorption isotherm of **NKU-200-Tb** for CO_2 at 298 K.

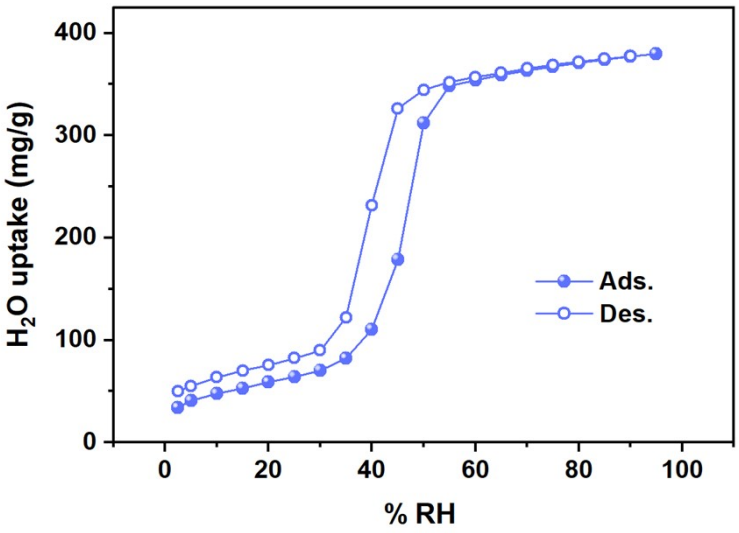

Fig. S14 The water vapor adsorption-desorption isotherm of **NKU-200-Tb** at 298 K.

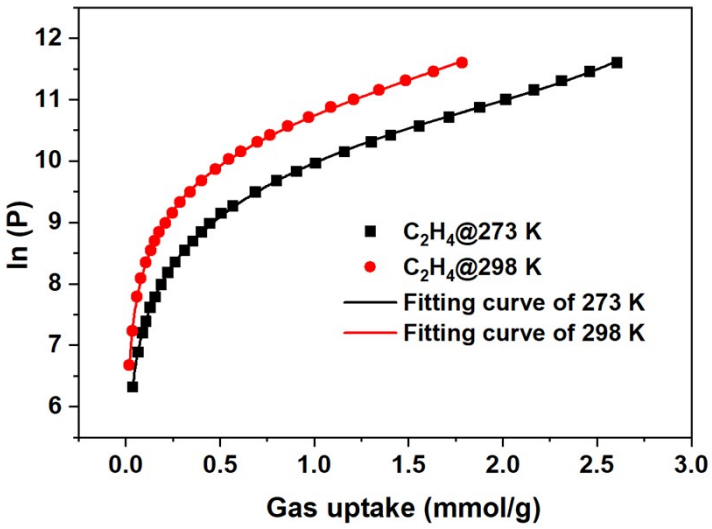

Fig. S15 Virial equation fitting of C_2H_4 adsorption isotherm of **NKU-200-Tb** at 273 and 298 K respectively. The fitting parameters are listed in Table S4.

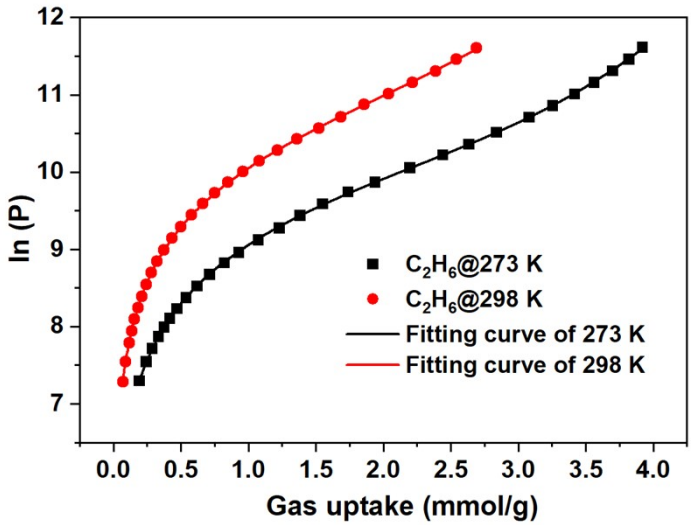

Fig. S16 Virial equation fitting of C_2H_6 adsorption isotherm of **NKU-200-Tb** at 273 and 298 K respectively. The fitting parameters are listed in Table S4.

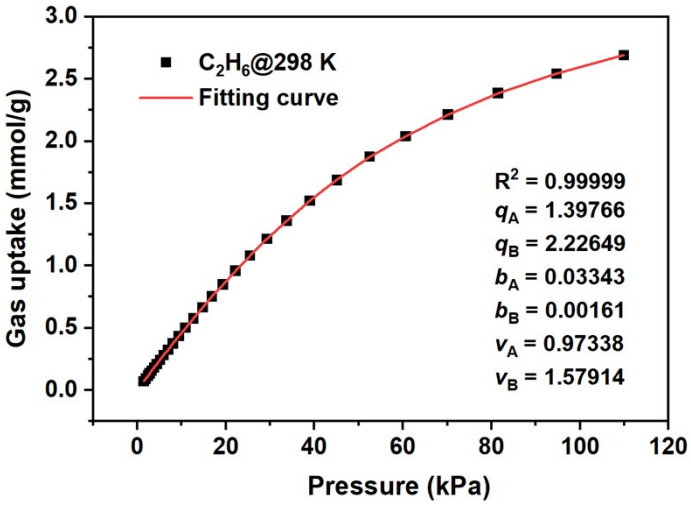

Fig. S17 Dual-site Langmuir-Freundlich fitting of C_2H_6 adsorption isotherm at 298 K and 1 bar for **NKU-200-Tb**.

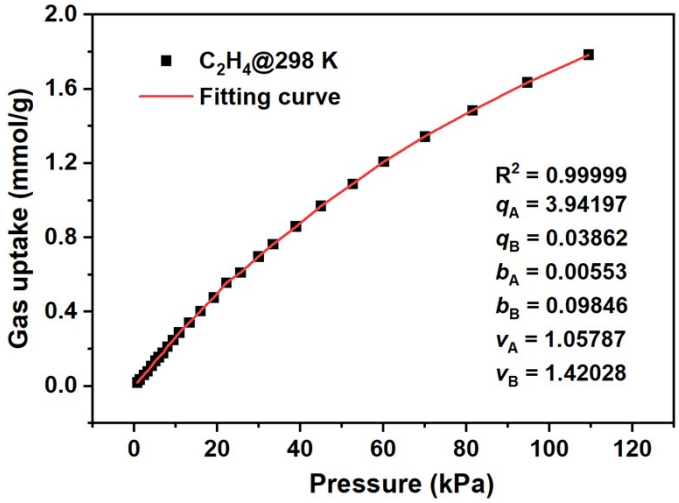

Fig. S18 Dual-site Langmuir-Freundlich fitting of C_2H_4 adsorption isotherm at 298 K and 1 bar for **NKU-200-Tb**.

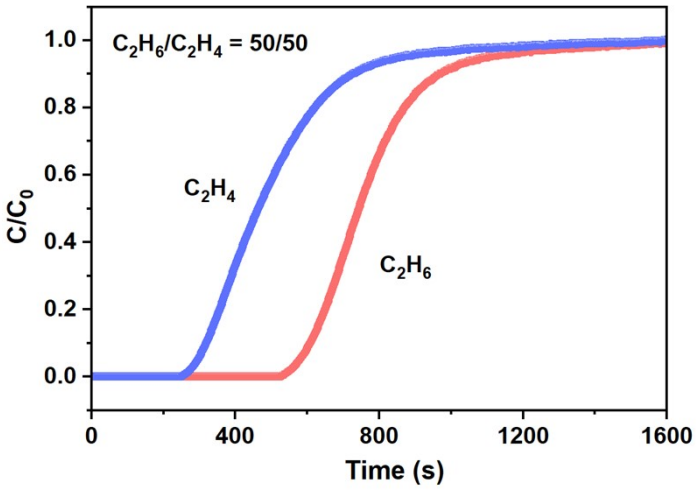

Fig. S19 Dynamic breakthrough curves for a binary C_2H_6/C_2H_4 (50/50, v/v) mixture at 298 K and 1 bar, with a total flow rate of 10.0 mL/min using He as the carrier gas (80%, vol%).

Tables.

Table S1 Crystal data and structure refinement parameters for **NKU-200-Tb**.

Compound	**NKU-200-Tb**
CCDC number	2177636
Chemical formula	$C_{90}H_{81}Tb_9O_{48}$
Crystal system	trigonal
Space group	$P\bar{3}$
a/(Å)	19.5608(17)
b/(Å)	19.5608(17)
c/(Å)	12.5307(18)
α/(°)	90
β/(°)	90
γ/(°)	120
V/(Å$^{3)}$	4152.2(9)
Z	1
D/(g/cm^3)	1.344
T/K	193.0
F(000)	1590
Goodness-of-fit on F^2	1.070
R_1 [I >2σ(I)][a]	0.0748
R_1 [all data][a]	0.0832
wR_2 [I >2σ(I)][b]	0.2252
wR_2 [all data] [b]	0.2331

[a]$R_1 = \sum||F_o| - |F_c|| / \sum|F_o|$; [b]$wR_2 = [\sum[w(F_o^2 - F_c^2)^2] / \sum w(F_o^2)^2]^{1/2}$.

Table S2 Summary of the stability of some representative C_2H_6-selective adsorbents.

Adsorbents	Hydrolytic stability	Thermal stability	Ref.
NKU-200-Tb	stable	500 °C	This work
LIFM-63	-	475 °C	11
NUM-7a	-	400 °C	12
NKMOF-8-Me	stable	400 °C	13
NKMOF-8-Br	stable	400°C	13
$Fe_2(O_2)$(dobdc)	unstable	-	14
PCN-250	stable	400 °C	15
$Ni(bdc)(ted)_{0.5}$	unstable	400 °C	16
Zn(ad)(int)	stable	300 °C	17
JNU-2	stable	350 °C	18
MUF-15	unstable	400 °C	19
IRMOF-8	-	420 °C	20
CPM-233	unstable	450 °C	21
$Ca(H_2tcpb)$	stable	400 °C	22
ZJU-120a	unstable	300 °C	23
$Cu(Qc)_2$	stable	280 °C	24
UiO-66	stable	500 °C	25
UiO-NDC	-	500 °C	25
UiO-67-$(NH_2)_2$	-	400 °C	26

- means the information was not given.

Table S3 Summary of adsorption metrics of some leading C_2H_6-selective adsorbents at 298 K and 1 bar.

Adsorbents	Uptake (mmol/g)		Uptake ratio (298 K, 1 bar)	Selectivity (50/50, v/v)	Q_{st} (kJ/mol)	Ref.
	C_2H_6	C_2H_4	C_2H_6/C_2H_4	C_2H_6/C_2H_4	C_2H_6	
NKU-200-Tb	2.69	1.78	151%	2.06	27.54	This work
LIFM-63	2.89	2.07	140%	1.56	26.5	11
NUM-7a	2.85	2.62	109%	1.76	35.8	12
NKMOF-8-Me	4.82	4.67	103%	1.88	38.4	13
NKMOF-8-Br	4.62	3.67	126%	2.65	40.8	13
$Fe_2(O_2)$(dobdc)	3.03	1.9	159%	4.4	66.8	14
PCN-250	5.21	4.22	123%	1.9	23.6	15
$Ni(bdc)(ted)_{0.5}$	5.0	3.4	147%	1.85	21.5	16
Zn(ad)(int)	2.32	2.09	111%	2.4	33	17
JNU-2	4.11	3.62	114%	1.6	30	18
MUF-15	4.69	4.15	113%	1.96	29.2	19
IRMOF-8	4.00	3.20	125%	1.75	52.5	20
CPM-233	7.45	6.52	114%	1.64	27.3	21
$Ca(H_2tcpb)$	2.78	2.67	104%	1.75	35	22
ZJU-120a	4.91	3.93	125%	2.74	27.6	23
$Cu(Qc)_2$	1.85	0.78	237%	3.4	28.8	24
UiO-66	2.3	1.7	135%	1.9	53	25
UiO-NDC	4.3	3.45	125%	1.35	58	25
UiO-67-$(NH_2)_2$	5.32	4.32	123%	1.7	26.5	26

Table S4 The fitted parameters of the virial equation for **NKU-200-Tb**.

Parameters	C_2H_6	C_2H_4
a_0	-3314.86084	-3006.06615
a_1	269.4333	756.90103
a_2	-165.7641	-307.85224
a_3	-8.63562	-15.15898
a_4	2.29724	5.58932
b_0	14.15769	13.71377
b_1	-0.87855	-2.40936
b_2	0.65936	1.14796
Adj. R-Square	0.99993	0.99986

References.

[1] G. M. Sheldrick, Crystal structure refinement with SHELXL, *Acta Crystallogr., Sect. C: Struct. Chem.,* 2015, **71**, 3–8.

[2] A. L. Spek, Structure validation in chemical crystallography, *Acta Crystallogr., Sect. D: Biol. Crystallogr.,* 2009, **65**, 148–155.

[3] M. G. Rabbani, A. K. Sekizkardes, O. M. El-Kadri, B. R. Kaafarani and H. M. El-Kaderi, Pyrene-directed growth of nanoporous benzimidazole-linked nanofibers and their application to selective CO_2 capture and separation, *J. Mater. Chem.*, 2012, **22**, 25409–25417.

[4] J. VandeVondele, M. Krack, F. Mohamed, M. Parrinello, T. Chassaing and J. Hutter, Quickstep: fast and accurate density functional calculations using a mixed Gaussian and plane waves approach, *Comput. Phys. Commun.*, 2005, **167**, 103–128.

[5] S. Goedecker, M. Teter and J. Hutter, Separable dual-space gaussian pseudopotentials, *Phys. Rev. B*, 1996, **54**, 1703–1710.

[6] C. Hartwigsen, S. Goedecker and J. Hutter, Relativistic separable dual-space gaussian pseudopotentials from H to Rn, *Phys. Rev. B*, 1998, **58**, 3641-3662.

[7] M. Krack and M. Parrinello, All-electron ab-initio molecular dynamics. *Phys. Chem. Chem. Phys.*, 2000, **2**, 2105-2112.

[8] J. VandeVondele and J. Hutter, Gaussian basis sets for accurate calculations on molecular systems in gas and condensed phases, *J. Chem. Phys.*, 2007, **127**, 114105.

[9] J. P. Perdew, K. Burke and M. Ernzerhof, Generalized gradient approximation made simple, *Phys. Rev. Lett.*, 1996, **77**, 3865–3868.

[10] S. Grimme, J. Antony, S. Ehrlich and H. Krieg, A consistent and accurate ab initio parametrization of density functional dispersion correction (DFT-D) for the 94 elements H-Pu, *J. Chem. Phys.*, 2010, **132**, 154104.

[11] C. X. Chen, Z. W. Wei, T. Pham, P. C. Lan, L. Zhang, K. A. Forrest and S. Chen, Nanospace engineering of metal–organic frameworks through dynamic spacer installation of multifunctionalities for efficient separation of ethane from ethane/ethylene mixtures, *Angew. Chem. Int. Ed*., 2021, **60**, 9680–9685.

[12] F. Z. Sun, S. Q. Yang, R. Krishna, Y. H. Zhang, Y. P. Xia and T. L. Hu, Microporous metal–organic framework with a completely reversed adsorption relationship for C_2 hydrocarbons at room temperature, *ACS Appl. Mater. Interfaces,* 2020, **12**, 6105–6111.

[13] S. B. Geng, E. Lin, X. Li, W. S. Liu, T. Wang, Z. F. Wang, D. Sensharma, S. Darwish, Y. H. Andaloussi, T. Pham, P. Cheng, M. J. Zaworotko, Y. Chen and Z. J. Zhang, Scalable room-temperature synthesis of highly robust ethane-selective metal–organic frameworks for efficient ethylene purification, *J. Am. Chem. Soc*., 2021, **143**, 8654–8660.

[14] L. B. Li, R. B. Lin, R. Krishna, H, Li, S. C. Xiang, H. Wu, J. P. Li, W. Zhou and B. L. Chen, Ethane/ethylene separation in a metal-organic framework with iron-peroxo sites, *Science,* 2018, **362**, 443–446.

[15] Y. W. Chen, Z. W. Qiao, H. X. Wu, D. F. Lv, R. F. Shi, Q. B. Xia, J. Zhou and Z. Li, An ethane-trapping MOF PCN-250 for highly selective adsorption of ethane over ethylene, *Chem. Eng. Sci*., 2018, **175**, 110–117.

[16] W. Liang, F. Xu, X. Zhou, J. Xiao, Q. Xia, Y. Li and Z. Li, Ethane selective adsorbent Ni(bdc)(ted)$_{0.5}$ with high uptake and its significance in adsorption separation of ethane and ethylene, *Chem. Eng. Sci*., 2016, **148**, 275–281.

[17] Q. Ding, Z. Q. Zhang, Y. L. Liu, K. G. Chai, R. Krishna and S. Zhang, One-step ethylene purification from ternary mixtures in a metal–organic framework with customized pore chemistry and shape, *Angew. Chem. Int. Ed.,* 2022, **61**, e202208134.

[18] H. Zeng, X. J. Xie, M. Xie, Y. L. Huang, D. Luo, T. Wang, Y. Zhao, W. Lu and D. Li, Cage-interconnected metal–organic framework with tailored apertures for efficient C_2H_6/C_2H_4 separation under humid conditions, *J. Am. Chem. Soc*., 2019, **141**, 20390–20396.

[19] O. T. Qazvini, R. Babarao, Z. L. Shi, Y. B. Zhang and S. G. Telfer, A robust ethane-trapping metal–organic framework with a high capacity for ethylene purification, *J. Am. Chem. Soc*., 2019, **141**, 5014–5020.

[20] J. Pires, M. L. Pinto and V. K. Saini, Ethane selective IRMOF-8 and its significance in ethane–ethylene separation by adsorption, *ACS Appl. Mater. Interfaces,* 2014, **6**, 12093–12099.

[21] H. Yang, Y. Wang, R. Krishna, X. Jia, Y. Wang, A. N. Hong, C. Dang, H. E. Castillo, X. Bu and P. Feng, Pore-space-partition-enabled exceptional ethane uptake and ethane-selective ethane–ethylene separation, *J. Am. Chem. Soc*., 2020, **142**, 2222–2227.

[22] Y. Lin, Y. Li, H. Wang, D. Luo, F. Lin and J. Li, Separation of ethane and ethylene by a robust ethane-selective calcium-based metal–organic framework, *New J. Chem*., 2020, **44**, 11933–11936.

[23] J. Pei, J. X. Wang, K. Shao, Y. Yang, Y. Cui, H. Wu, W. Zhou, B. Li and G. Qian, Engineering microporous ethane-trapping metal–organic frameworks for boosting ethane/ethylene separation, *J. Mater. Chem. A,* 2020, **8**, 3613–3620.

[24] R. B. Lin, H. Wu, L. Li, X. L. Tang, Z. Li, J. Gao, H. Cui, W. Zhou and B. Chen, Boosting ethane/ethylene separation within isoreticular ultramicroporous metal–organic frameworks, *J. Am. Chem. Soc*., 2018, **140**, 12940–12946.

[25] J. Pires, J. Fernandes, K. Dedecker, J. R. B. Gomes, G. Pérez-Sánchez, F. Nouar, C. Serre and M. L. Pinto, Enhancement of ethane selectivity in ethane–ethylene mixtures by perfluoro groups in Zr-based metal–organic frameworks, *ACS Appl. Mater. Interfaces,* 2019, **11**, 27410–27421.

[26] X. W. Gu, J. X. Wang, E. Y. Wu, H. Wu, W. Zhou, G. D. Qian, B. L. Chen and B. Li, Immobilization of lewis basic sites into a stable ethane-selective MOF enabling one-step separation of ethylene from a ternary mixture, *J. Am. Chem. Soc*., 2022, **144**, 2614–2623.